Pressure Tuning of Coupled Structural and Spin State Transitions in the Molecular Complex [Fe(H 2 B(pz) 2) 2 (phen)]

Damian Paliwoda, Laure Vendier, William Nicolazzi, Gábor Molnár, Azzedine Bousseksou

Pressure Tuning of Coupled Structural and Spin State Transitions in the Molecular Complex [Fe($H_2B(pz)_2)_2$(phen)]

Damian Paliwoda, Laure Vendier, William Nicolazzi, Gábor Molnár*, Azzedine Bousseksou*

LCC, CNRS & Université de Toulouse (UPS, INP), 31077 Toulouse, France

Abstract. The large volume change, which accompanies the molecular spin crossover (SCO) phenomenon in some transition metal complexes, prompts also frequently the coupling of the SCO with other instabilities. Understanding the driving mechanism(s) of such coupled phase transitions is not only important for fundamental reasons, but provides also scope for the development of multifunctional materials. The general theoretical expectation is that the coupling has elastic origin and the sequence of transitions can be tuned by an externally applied pressure, but dedicated experiments remain scarce. Here, we used high pressure and low temperature single-crystal x-ray diffraction to investigate the high-spin (HS) to low-spin (LS) transitions in the molecular complexes [$Fe^{II}(H_2B(pz)_2)_2$(bipy)] and [$Fe^{II}(H_2B(pz)_2)_2$(phen)]. In the bipyridine complex the SCO is continuous and isostructural over the whole *T, P*-range (100-300 K, 0-2 GPa). In the phenanthroline derivative, however, the SCO is concomitant with a symmetry-breaking transition (*C*2/*c* to $P\bar{1}$). Structural analysis reveals that the coupling between the two phenomena can be tuned by external pressure from a virtually simultaneous $HS_{C2/c}$ - $LS_P\bar{1}$ transition to the sequence of $HS_{C2/c}$ - $LS_{C2/c}$ - $LS_P\bar{1}$ transitions. The correlation of spontaneous strain and order parameter behaviors highlights that the 'separated' transitions remain still connected via strain coupling, whereas the 'simultaneous' transitions are partially split.

INTRODUCTION

Coupled phase transitions, driven concurrently by different physical phenomena (atomic ordering, soft modes, spin state transitions, ferroic ordering, etc.), are widespread in crystalline solids and have been investigated in various fields of physics, chemistry, mineralogy and materials science.[1-11] Since phase transitions in crystalline materials always involve some lattice distortion, the most common physical effect that couples them is lattice strain.[12] In this context, spin state transitions in molecular complexes of $3d^4$-$3d^7$ ions appear particularly interesting due to the large volume strains involved (typically 1-10 %).[13-18] Thanks to this high dilation, the SCO phenomenon can strongly couple to various instabilities, leading to a great diversity of structure-property relationships. Among the numerous reported examples (see for example Refs. 7 and 19 and references therein), we can mention here the benchmark complexes $[Fe^{II}(ptz)_6](BF)_4$ (ptz = 1-n-propyl-tetrazole), in which the SCO is coupled to a ferroelastic transition,[20-21] and $[Fe^{II}(2\text{-pic})_3]Cl_2 \cdot EtOH$ (pic = picolylamine), in which the SCO is coupled to successive order-disorder transitions.[22]

In the spin crossover literature the problem of coupled phase transitions is often evoked in relation with the question, which phenomenon drives the other (*sic* the 'chicken and egg' problem). As discussed by Hauser et al.[23], this is possibly just "the wrong question to ask" whenever the contributions of the transitions to the free energy are of similar orders of magnitude. Instead, such coupled transitions should better analyzed by (1) setting up the Gibbs free energy for each physical phenomena (uncoupled), (2) establishing the coupling terms between them and (3) examining the consequences of this coupling on the physical behavior of the material (e.g. response to external stimuli) both experimentally and theoretically. The latter has been achieved using various methods, including the Slichter-Drickamer regular solution approach,[23-25] microscopic models[26-31] and the Landau theory[19,32]. In particular, the Landau

approach provided a very useful tool for exploring the phase diagrams for the most common coupling schemes in SCO materials.[33]

Coupling of SCO with other instabilities is not only of fundamental interest, but represents also an interesting scope for the development of a variety of multifunctional SCO materials with liquid crystal,[34] ferroelectric,[35] multiferroic[36] and other interesting properties[37-40] – just to mention a few representative cases. For example, a detailed investigation of an Mn^{III} SCO complex revealed that coupling between the SCO and symmetry-breaking structural transitions gives rise to significant changes of the electrical polarization simultaneously with the SCO, witnessed as a magneto-electric coupling.[36] It is fair to say, however, that designing single-phase SCO materials with coupled phase transitions is difficult and this research is driven largely by serendipity. Notable examples for more 'rational' strategies include the synthesis of SCO complexes with long alkyl chains, potentially affording coupled SCO and liquid crystal (or melting) transitions[34,41-43] and SCO complexes with Jahn-Teller ions (e.g. Mn^{III}), providing scope for coupled ferroelastic/ferroelectric transitions[44].

On the other hand, tuning the sequence of the transitions is more straightforward. Chemical tuning can be achieved most conveniently by the 'chemical pressure' method, based on the isomorphous substitution of the SCO cation with metal ions of different radii.[23] Introduction of counter-anions of different size[45] or guest molecules[46] might also play a similar role in some cases. Alternatively, one can also apply an external hydrostatic pressure. The expectation is that the respective phase transition temperatures do not shift to the same extent under pressure (chemical or external) and therefore the sequence of transitions must be altered.[47-48]

X-ray (or neutron) diffraction under pressure appears here as a particularly attractive experimental means to investigate the coupling of SCO phenomenon to other transitions.[49] Although such investigations on SCO compounds, which are often of low symmetry, remain

challenging,[50-66] they have already given valuable insights into the sequence of coupled phase transitions in a few cases.[67-77] Here we focus on the high-pressure single-crystal X-ray diffraction (HP-SC-XRD) technique, which not only allows for tuning the transitions, but provides also an accurate measure of the spin-state change, reflected by metal-ligand bond lengths, and the lattice deformations associated with the different transitions. Eventually, it can thus afford for a thermodynamic description of the elastic (strain) coupling mechanism.

In this work, we use the HP-SC-XRD approach to investigate two closely related SCO complexes $[Fe^{II}(H_2B(pz)_2)_2(bipy)]$ **(1)** (pz = pyrazol-1-yl, bipy = 2,2'-bipyridine) and $[Fe^{II}(H_2B(pz)_2)_2(phen)]$ **(2)** (phen = 1,10-phenanthroline) (Figure 1), which are both known to undergo thermal SCO centered around 160-170 K (at 1 atm)[78-79] and pressure-induced SCO centered around 0.7-0.9 GPa (at 293 K)[80]. Crucially, however, the thermal SCO in **(1)** is isostructural, whereas in **(2)** it is associated with a symmetry breaking transition,[81] providing thus 'textbook examples' for pure and coupled SCO phenomena.

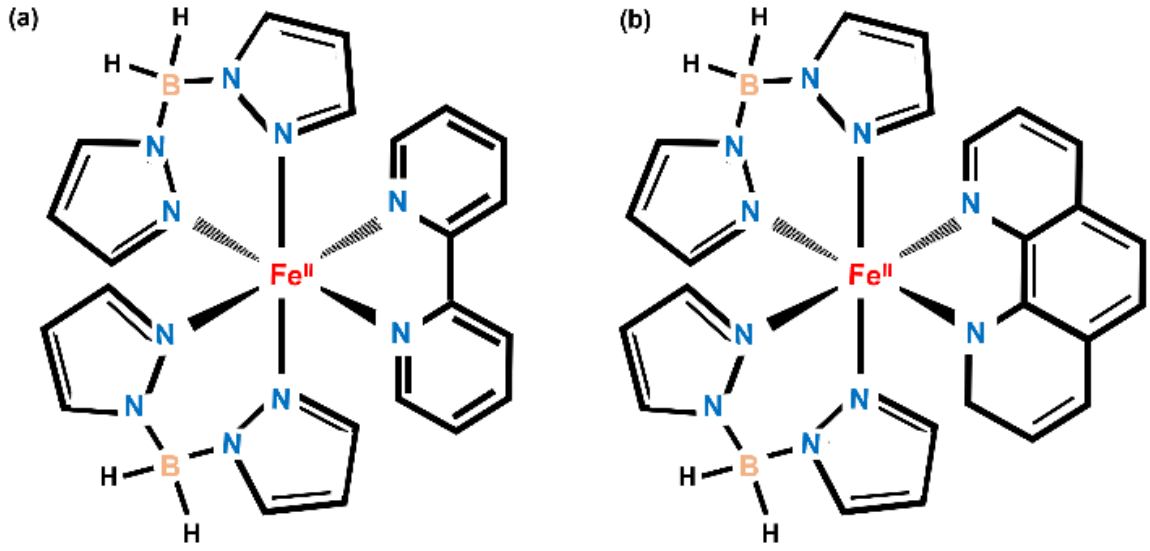

Figure 1. Schematic representation of the molecular structures of (a) compound **(1)** and (b) compound **(2)**.

EXPERIMENTAL METHODS

Crystals of **(1)** and **(2)** have been synthesized and grown according to previously described procedures.[78-79] SC-XRD data were collected using a XtaLAB Synergy-S Rigaku diffractometer equipped with hybrid photon counting Hypix-6000HE detector and two microsources, Mo (λ = 0.71073 Å), used in high pressure measurements, and Cu (λ = 1.5406 Å), used for low temperature data collection. Low-temperature measurements have been conducted between 100 K and 300 K using an Oxford Cryosystems 800 Cryostream Cooler Device. High-pressure diffraction experiments have been performed at room temperature using a One20DAC Almax-EasyLab wide-angle diamond anvil cell (DAC) equipped with diamonds of Boehler-Almax design and of a cullet diameter of 800 μm. Stainless steel gaskets of 0.15 mm thickness with holes of *ca.* 0.4 mm in diameter have been prepared by spark-erosion. The fluoresecence of ruby was used as a pressure gauge[82] and Daphne 7373 oil as the pressure-transmitting medium – providing hydrostatic conditions up to *ca.* 2.2 GPa.[83] The CrysAlisPro program suite was used for pre-experiment, DAC alignment, data collection, determination of the UB matrices and initial data reduction.[84] Crystal structures of **(1)** and **(2)** were solved and refined using SHELXS and SHELXL programs.[85] Hydrogen atoms were located from geometry after each refinement cycle with $U_{iso} = 1.2U_{eq}$ of their carriers.

RESULTS

Evidence for transformations from optical micrographs. Initial variable-temperature, polarized-light optical microscopy observations of crystals of **(1)** revealed a gradual and homogeneous crossover between the HS and LS phases in the temperature range of *ca.* 150 – 180 K (Figure 2, top panel), confirming thus the continuous character of the SCO, which was postulated from previous magnetic measurements.[79] On the contrary, crystals of **(2)** exhibited a discontinuous phase transition, proceeding by nucleation and growth. As an example, Figure 2

(bottom panel) presents micrographs captured at a constant temperature (163 K) wherein the advance of the phase front(s) is clearly observable (see Movies S1 and S2 for a complete heating-cooling cycle in the Supporting Information, SI). The phase fronts were found to form reproducibly on both sides of the crystal (left and right in the photos) and, at the same time, the size, shape and position of the crystal slightly changed. The strong darkening of the crystal in the low-temperature phase must be ascribed to the change of electronic state (HS to LS), indicating thus its first-order nature. This finding is in good agreement with previously reported magnetic measurements on polycrystalline samples of **(2)**, showing thermal hysteresis of the magnetic susceptibility.[79] On the other hand, in our experimental conditions, we have found no evidence for the formation of ferroelastic domains, which might be anticipated in the low-symmetry phase.[86] We note also that similar color changes were observed in the crystals at low temperatures and high pressures (not shown), but the nature of the pressure-induced transitions could not be assessed from optical microscopy observations.

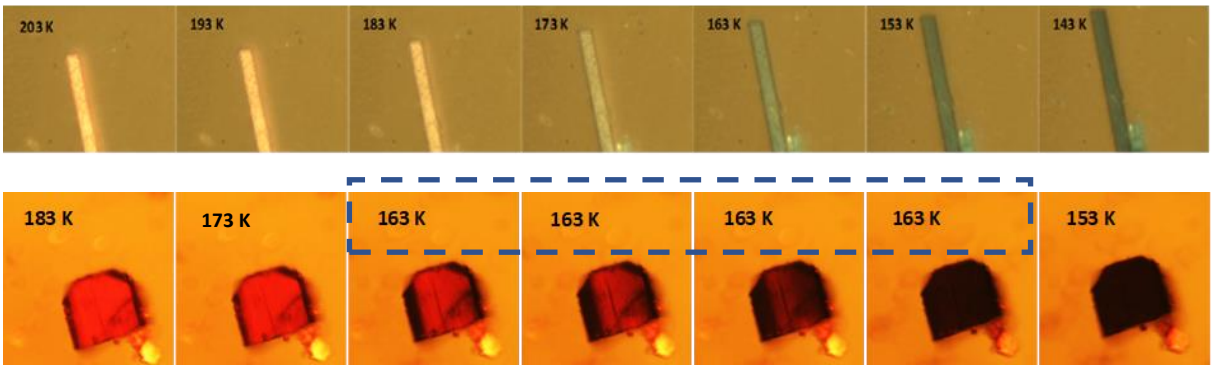

Figure 2. Reflected light optical micrographs of crystals of **(1)** (top panel) and **(2)** (bottom panel) at selected temperatures under crossed polarizers.

Low-temperature and high-pressure crystal structures. Variable temperature structural resolutions of **(1)** and **(2)** have been performed at eleven individual temperature points between 100 K and 300 K at atmospheric pressure and nine individual pressure points up to ca. 2 GPa at ambient temperature. Importantly, both the temperature and pressure effects were found fully

reversible. (Details of the refinement, crystal structures and lattice parameters are given in Tables S1-S4 in the SI.)

The coordination sphere and the central atom environment in **(1)** and **(2)** adopts distorted octahedral symmetry with FeN_6 core (see Tables S5-S8). In both cases, the unit-cell contains two pairs of chiral molecules, right- and left-handed complex enantiomers. The central Fe(II) ion is coordinated by three chelating N-donor ligands: two negatively charged bis(1-pyrazolyl)borate ligands and one nearly planar 2,2'-bipyridine or one planar phenanthroline ligand in complex **(1)** and **(2)**, respectively. In the solid state, the molecules of **(1)** are linked by weak CH---C, CH—HB and π-π stacking interactions present in both spin states. In the case of **(2)**, one can note the presence of CH---C and π-π stacking interactions in the LS state, whereas only weak CH---C contacts have been found in the HS state (see Figure 3 and Tables S9-S12 in SI). We can thus tentatively suggest that a possible driving force of the structural transition in **(2)**, in opposition to **(1)**, is a lattice deformation allowing for the creation of these intermolecular interactions.

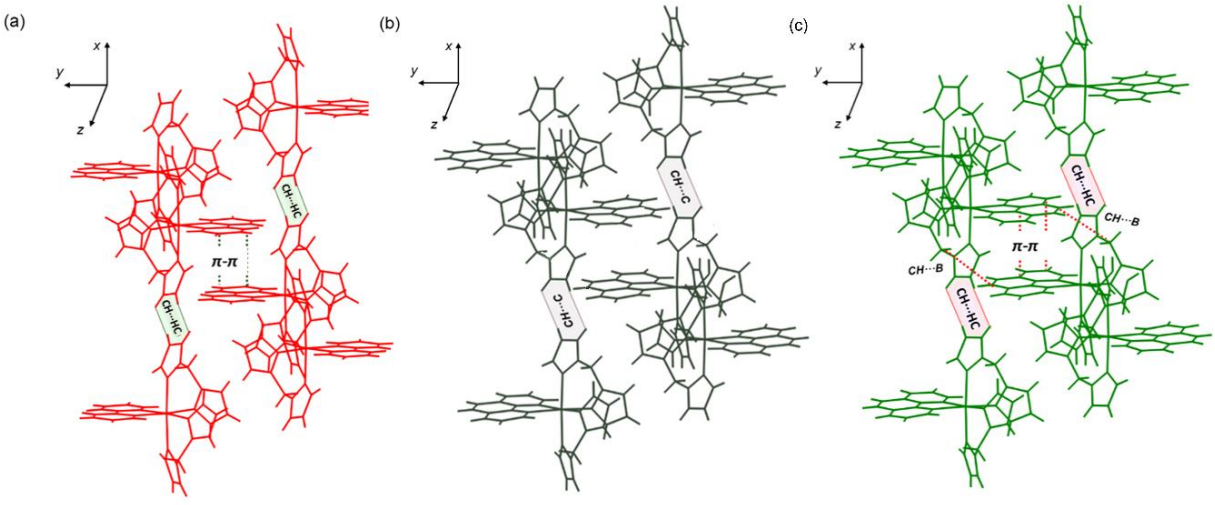

Figure 3. Intermolecular interactions in the HS and LS crystals of **(1)** (a), HS crystals of **(2)** (b) and LS crystals of **(2)** (c).

In agreement with previous reports,[81] our low temperature XRD measurements on **(1)** revealed an isostructural SCO, which is associated with a significant elongation of the mean Fe-N distances from 2.001(4) Å at 100 K to 2.191(3) Å at 300 K (see Figure 4 and Table 1). Each structure was solved in the monoclinic space group *C2/c*, with half a molecule in the asymmetric unit. In contrast to **(1),** the phenanthroline derivative undergoes spin transition accompanied with a crystal symmetry change, manifested as a transition from a triclinic ($P\bar{1}$) LS to a monoclinic (*C*2/*c*) HS phase between ca. 160-180 K, resulting in the disappearance of superlattice reflections of the type *h0l, l=2n+1* in the monoclinic phase (see Figures S1-S4). The concomitant elongation of the average Fe-N distances is similar to compound **(1):** 1.999(2) Å at 100 K and 2.186(3) Å at 300 K (see Figure 4 and Table 1).

Table 1. Average Fe-N distances in **(1)** and **(2)** at selected temperatures and pressures. The spin state and the crystal structure are also indicated.

Compound	Spin state	Space group	Temperature	Pressure	av. Fe-N distances
(1)	LS	*C*2/*c*	100 K	ambient	2.001(4) Å
(1)	LS	*C*2/*c*	160 K	ambient	2.067(4) Å
(1)	HS	*C*2/*c*	180 K	ambient	2.160(4) Å
(1)	HS	*C*2/*c*	300 K	ambient	2.191(3) Å
(1)	HS	*C*2/*c*	ambient	0.41 GPa	2.176(2) Å
(1)	LS	*C*2/*c*	ambient	0.92 GPa	2.084(2) Å
(1)	LS	*C*2/*c*	ambient	2.01 GPa	1.991(2) Å
(2)	LS	$P\bar{1}$	100 K	ambient	1.999(2) Å
(2)	LS	$P\bar{1}$	160 K	ambient	2.032(3) Å
(2)	HS	*C*2/*c*	180 K	ambient	2.160(4) Å
(2)	HS	*C*2/*c*	300 K	ambient	2.186(3) Å
(2)	HS	*C*2/*c*	ambient	0.40 GPa	2.167(2) Å
(2)	LS	*C*2/*c*	ambient	0.73 GPa	2.040(5) Å
(2)	LS	$P\bar{1}$	ambient	0.88 GPa	1.98(1) Å
(2)	LS	$P\bar{1}$	ambient	2.15 GPa	1.962(9) Å

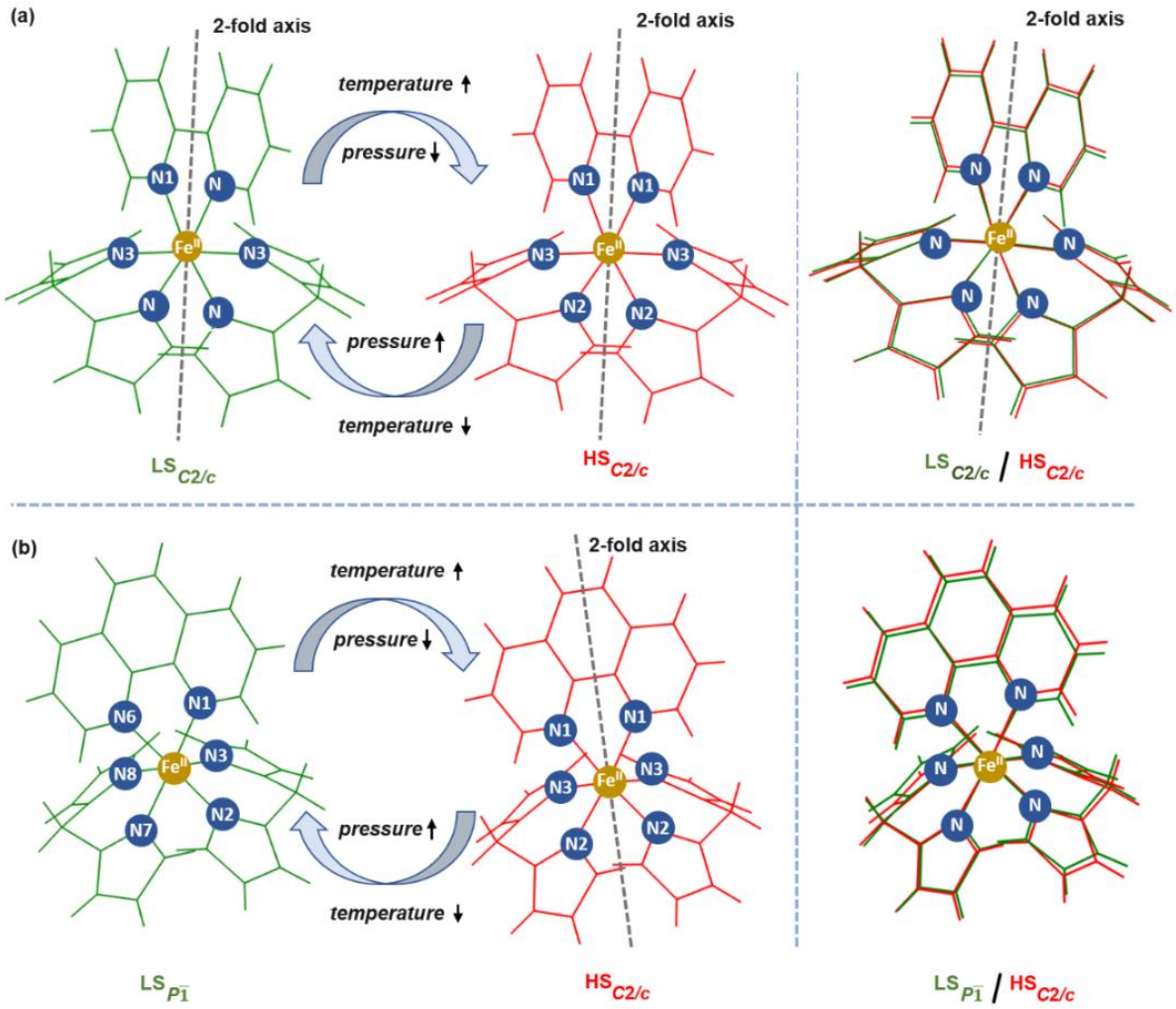

Figure 4. LS and HS structures of (a) **(1)** and (b) **(2)** and their overlays in the right panel.

In terms of SCO and structural changes, the pressure effects on **(1)** and **(2)** are similar to those observed at low temperatures (see Figure S5). The SCO in **(1)** under pressure is obviously manifested by the decrease of the mean Fe-N distance, reaching 1.991(2) Å at 2 GPa. Within this pressure range, no change of crystal symmetry could be observed. The key experimental result of the present work is the separation of the SCO and the structural transition in **(2)** under pressure. This finding is clearly manifested by a monoclinic LS structure at 0.73 GPa, displaying a mean Fe-N distance of 2.040(5) Å (see Table 1 and Figure S4). Further compression above 0.88 GPa results then in a separate structural phase transition from the monoclinic LS to the triclinic LS form. This stepwise sequence is reminiscent to those reported

for the compounds $[Fe(ptz)_6](BF)_4$ and $[Co(dpzca)_2]$ (dpzca = N-(2-pyrazylcarbonyl)-2-pyrazinecarboxamide) under pressure, although with the inversion between the sequence of the SCO and the symmetry breaking transitions (*vide infra*).[69,73] Of particular interest with respect to these previous studies is the direct observation of the intermediate phase with resolved atomic positions, allowing for the unambiguous assignments of the spin state and space group in the same time.

Lattice compressibility. Since the elastic properties of the lattice play a key role both in the SCO phenomenon and its coupling with the symmetry-breaking transition, it is important to assess the lattice compressibility from the HP-XRD data. The variations of the unit-cell volume and the individual lattice parameters with pressure follow the typical monotonic, nonlinear trend on compression for both compounds (Figure 5 and Tables S1-S2). The compressibility of the lattice masks the volume change associated with the pressure-induced SCO and hence full structure refinement is inevitable for the assessment of the spin state of the materials (see inset in Figure 5). Third order Birch–Murnaghan equations of state were fitted to the volume evolution of **(1)** and **(2)** with pressure using EosFit7.[87] In general, the fits for the different phases are limited to a relatively narrow pressure range and are restricted to a few data points, resulting in rather high uncertainties (see Figures S6-S7).

The bulk modulus of **(2)** in the HS state is 4.6(2) GPa, reflecting the soft nature of these molecular solids, in good agreement with elastic modulus values derived previously from nuclear inelastic scattering (NIS) measurements on a polycrystalline powder [88].[88] Due to the pressure-induced structural transition and the lack of ambient pressure data for the triclinic LS form, it was impossible to fit an appropriate EOS and extract its bulk modulus. However, the LS form of **(2)** seems to be less compressible than the HS phase, which is also witnessed through

the strong decrease of the volumetric thermal expansion coefficient from 2.04(5) × 10^{-4} K^{-1} to 1.4(1) × 10^{-4} K^{-1} when going from the HS to the (triclinic) LS phase.

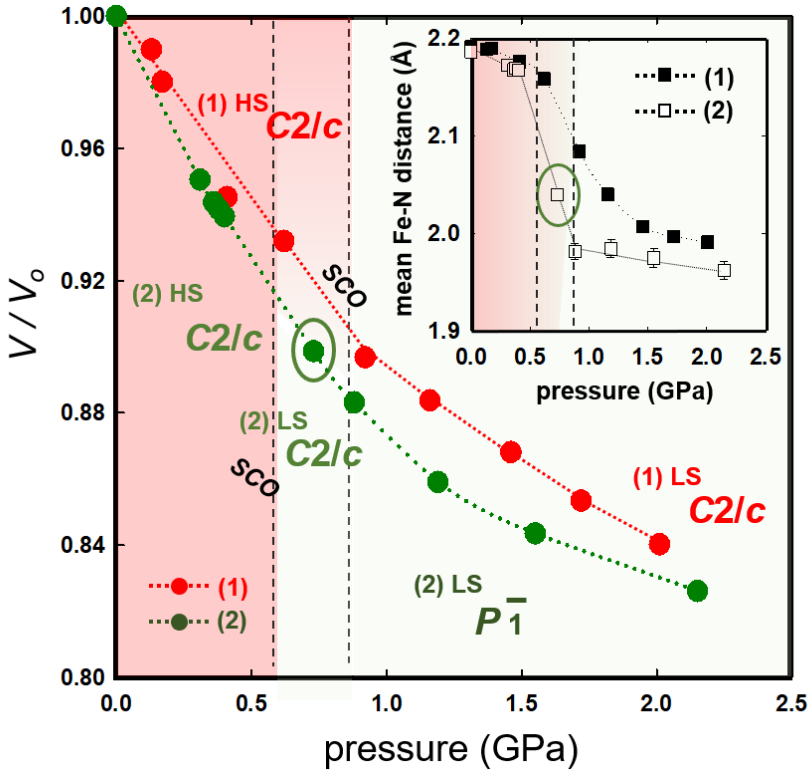

Figure 5. Pressure dependence of the unit cell volume (normalized to the atmospheric pressure volume) for **(1)** and **(2)**. The inset shows the average Fe-N distances for both compounds. The dotted lines are guides to the eye. The successive spin-state and structural transitions are indicated.

Crystals of **(1)** show similar volume compressibility with a bulk modulus of 6.0(5) GPa. Since the fit overlaps the region of SCO, this value should be considered only as an indication of the elastic properties of the lattice across the investigated pressure range, rather than a true equation of state. Nevertheless, one can qualitatively note in Figure 5 that there is less contrast between the compressibility of the HS and LS phases of **(1)**, which is also reflected by the smaller changes in thermal expansion coefficients (1.75(3) × 10^{-4} K^{-1} vs. 1.5(2) × 10^{-4} K^{-1} in the HS and

LS forms, respectively). It is noteworthy also that the compressional anisotropy of the different monoclinic forms remains moderate, whereas the triclinic LS phase of **(2)** displays pronounced anisotropy with the *a*-axis being nearly incompressible (see Tables S1-S2).

DISCUSSION

Strain coupling in (1) displaying non-symmetry-breaking SCO. Spontaneous strain variations were calculated from changes of the lattice parameters using the method (and the underlying Cartesian coordinate system) described by Carpenter et al.[12] (see the SI for more details). The spontaneous strain [ε_{ij}] is defined with respect to the lattice parameters the HS phase would have at the same temperature, i.e. it characterizes solely the SCO phenomenon without any background thermal effects. It forms a symmetric second rank tensor with six independent components, but the monoclinic symmetry of **(1)** reduces the number of strain components to four (ε_1, ε_2, ε_3 and ε_5 - in Voigt notation).[89] Figure 6a shows these strain components across the thermal SCO, which is centered at 165 K for **(1)**. The prevailing effect of SCO is *ca.* 3 % volume contraction in the LS state, which can be primarily accounted for the reduced radius of diamagnetic Fe^{II} ions. Noticeably, this volume strain V_s is strongly anisotropic ($Vs \approx \varepsilon_2 + \varepsilon_3$) and there is also a non-negligible shear component (~1 %). We note also the good agreement between the values of $V_s(T)$ obtained directly from the unit cell volume and calculated as $Vs = \varepsilon_1 + \varepsilon_2 + \varepsilon_3$, providing support for the strain analysis.

The total excess Gibbs free energy of the transition (ΔG) can be written as (see the SI for details):[86,33,90]

$$\Delta G = L(q_{spin}) + \frac{1-q_{spin}}{2}\sum_i \lambda_i \varepsilon_i + \frac{1}{2}\sum_{ij} C^{\circ}_{ij}\, \varepsilon_i \varepsilon_j \qquad (1)$$

where $L(q_{spin})$ is the Landau potential of the order parameter q_{spin}, λ_i are the strain - order parameter coupling coefficients and C°_{ij} are the relevant components of the elastic stiffness

matrix (in ambient conditions) and *i*,*j* = 1-3, 5 due to the monoclinic symmetry. In the case of the stress free crystal, $\frac{\partial(\Delta G)}{\partial \varepsilon_i} = 0$, and therefore:

$$\varepsilon_i = -\left(\frac{1-q_{spin}}{2}\frac{\lambda_i}{C^{\circ}_{ii}} + \frac{\sum_j C^{\circ}_{ij}\varepsilon_j}{C^{\circ}_{ii}}\right) \quad (2)$$

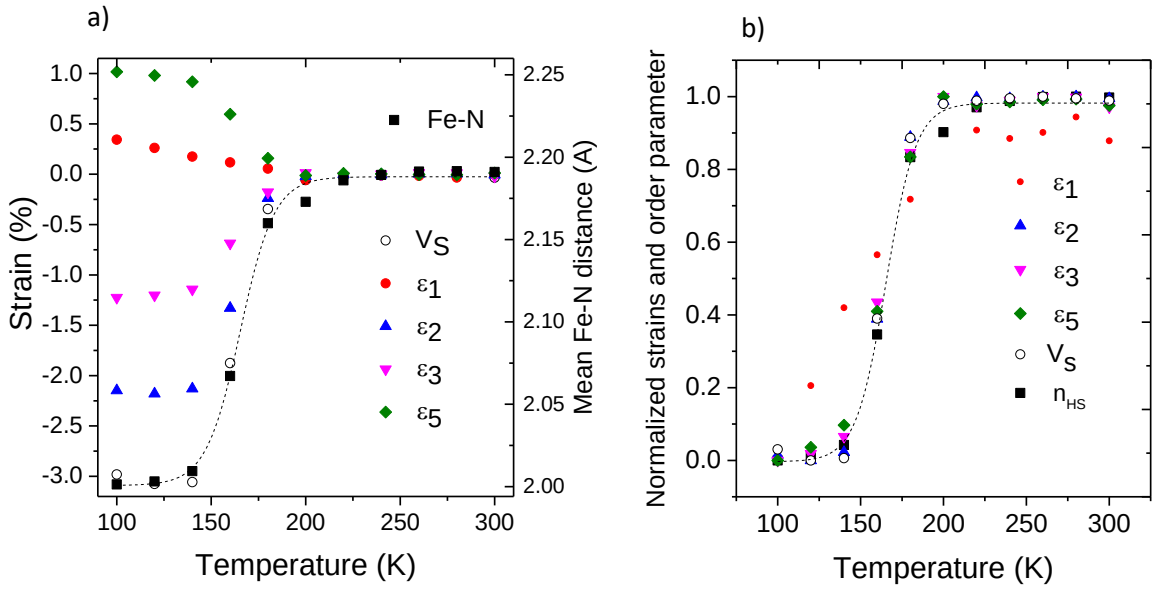

Figure 6. (a) Components of the spontaneous strain tensor (ε_i), volume strain (V_s) and mean Fe-N distance as a function of the temperature in the heating mode for compound **1**. b) Strain components rescaled to values of between 0 and 1 for comparison with the temperature variation of the HS fraction. (Lines are guides to the eye.)

The expectation must be that each component ε_i scales linearly with the order parameter ($\varepsilon_i \sim q_{spin}$). Here it is convenient that the structural resolution provides also the average Fe-N bond lengths, $\bar{d}_{FeN}$, at different temperatures, which can be directly used to characterize the temperature dependence of q_{spin}. As shown in Figure 6b, the normalized $\varepsilon_i(T)$ data superpose with the SCO curve (dotted line), confirming thus nicely the expected linear relationship between the order parameter and the spontaneous strain components expressed by Eq. 2. (*N.B.* The variation of ε_1 does not follow this trend, but this strain component is very weak (< 0.004)

and most likely dominated not by the SCO, but the thermal expansion mismatch of the HS and LS phases.)

Similar to the thermally induced SCO, the change of Fe-N bond lengths reveals unambiguously a complete HS to LS transition, centered around 0.9 GPa (see insert in Figure 5). The pressure shift of the spin transition (145 K/GPa) is in reasonably good agreement with previous magnetometry measurements under pressure (190 K/GPa),[80] taking into account the accuracy of the pressure gauges used. Due to the difficulties to subtract the compressibility of the lattice from pressure effects induced by the SCO, a reliable analysis of the spontaneous strain tensor was not possible under compression. Nevertheless, the ensemble of the structural data proves unambiguously the isostructural and continuous nature of the SCO in **(1)** in the investigated pressure and temperature range – in agreement with the description provided by Equation 1.

Strain coupling in (2) displaying a symmetry-breaking SCO. In contrast to the bipirydine analogue, the SCO behavior of the phenanthroline derivative is obviously complicated by the change in crystal system from monoclinic to triclinic both on decreasing temperature and increasing pressure. The description of this ferroelastic phase transition in **(2)** requires a second order parameter, q_{ferro} besides the SCO order parameter, q_{spin}. The active representation for the symmetry breaking process is B_g in the point group *2/m*,[86] giving $\varepsilon_4 \sim \varepsilon_6 \sim q_{ferro}$ as the expected strain - order parameter relationship. These strains can have a bilinear coupling thus with the order parameter q_{ferro}. Besides these two symmetry-breaking strains, ε_{sb}, associated with the ferroelastic transition, one would expect also the emergence of non-symmetry breaking strains, ε_{nsb}, ($\varepsilon_1 \sim \varepsilon_2 \sim \varepsilon_3 \sim \varepsilon_5$) associated with the SCO, all of which transform as the identity representation A_g of *2/m*, leading to bilinear coupling with q_{spin}. In addition, since both ${q^2}_{ferro}$ and ${\varepsilon^2}_i$ transform as the identity representation, linear – quadratic coupling terms of the form

$\varepsilon_{nsb}q^2{}_{ferro}$ and $\varepsilon^2{}_{sb}q_{spin}$ are also symmetry allowed. In a first approximation, however, we neglect the higher order terms. Then, the total excess Gibbs free energy of the transition in **(2)** can be written as (see the SI for further discussion):

$$\Delta G = L(q_{ferro}) + q_{ferro}(\lambda_4\varepsilon_4 + \lambda_6\varepsilon_6) + q^2{}_{ferro}(\lambda_1\varepsilon_1 + \lambda_2\varepsilon_2 + \lambda_3\varepsilon_3 + \lambda_5\varepsilon_5) +$$

$$+L(q_{spin}) + \frac{1-q_{spin}}{2}(\lambda_{1s}\varepsilon_1 + \lambda_{2s}\varepsilon_2 + \lambda_{3s}\varepsilon_3 + \lambda_{5s}\varepsilon_5) + \frac{1}{2}\sum_{ij} C^{\circ}_{ij}\,\varepsilon_i\varepsilon_j \quad (3)$$

Using this full potential is tedious; therefore, we will restrict our discussion for the following simplified form, which keeps the essential physical ingredients:

$$\Delta G = L(q_{ferro}) + q_{ferro}\lambda_{sb}\varepsilon_{sb} + q^2{}_{ferro}\lambda_{nsb1}\varepsilon_{nsb} + L(q_{spin}) + \frac{1-q_{spin}}{2}\lambda_{nsb2}\varepsilon_{nsb} +$$

$$+\sum_{ij} C^{\circ}_{ij}\,\varepsilon_i\varepsilon_j \quad (4)$$

At mechanical equilibrium ($\frac{\partial(\Delta G)}{\partial\varepsilon_{nsb}} = 0$, $\frac{\partial(\Delta G)}{\partial\varepsilon_{sb}} = 0$), one obtains (similar to eq. 2):

$$\varepsilon_{nsb} = -\left(q^2{}_{ferro}\frac{\lambda_{nsb1}}{K} + \frac{1-q_{spin}}{2}\frac{nsb2}{K}\right) \quad (5a)$$

$$\varepsilon_{sb} = -q_{ferro}\frac{\lambda_{sb}}{C^{\circ}} \quad (5b)$$

Substituting these results back to equation 4 and using the Landau expansion[91,33] gives:

$$\Delta G = \frac{1}{2}a_1\left(T - T_{ferro} - \frac{\lambda_{sb}{}^2}{2C^{\circ}a_1} - \frac{\lambda_{nsb1}\lambda_{nsb2}}{4Ka_1}\right)q^2{}_{ferro} + \frac{1}{4}\left(b - \frac{\lambda_{nsb1}{}^2}{2K}\right)q^4{}_{ferro} +$$

$$+ \frac{1}{4}cq^6{}_{ferro} + A_1[T - T_{SCO} + \frac{\lambda_{nsb2}{}^2}{2A_1K}]q_{spin} + \frac{1}{2}(B - \frac{\lambda_{nsb2}{}^2}{4K})q^2{}_{spin} + \frac{1}{4}Cq^4{}_{spin} +$$

$$+ \left(\frac{\lambda_{nsb1}\lambda_{nsb2}}{4K}\right)q^2{}_{ferro}q_{spin} \quad (6)$$

Equation 6 highlights that strain couplings lead to the increase of both transition temperatures and make the transitions more cooperative through the decrease of the values of *b* and *B*. (*N.B.* Obviously, both λ^2 and *K* take positive values, whereas a_1 (resp. A_1) is in general positive (resp. negative).[32-33]) In addition, the lattice strains give rise to a linear-quadratic coupling term, $q^2{}_{ferro}q_{spin}$, which has been already discussed for similar transitions with coupled symmetry-breaking and non-symmetry-breaking order parameters.[8-9,19,32-33,92]

The temperature dependence of selected spontaneous strain tensor components of **(2)** are shown in Figure 7a (see Figure S8 for the full tensor). Two series of data are traced together: one with 20 K steps including full structure resolutions and another with small steps (down to 2 K in the vicinity of the transition) affording only for unit cell parameters. In order to facilitate the comparison between the monoclinic and triclinic lattices, the strain components were calculated using the lattice parameters of the triclinic reduced cells (see Figure S9).

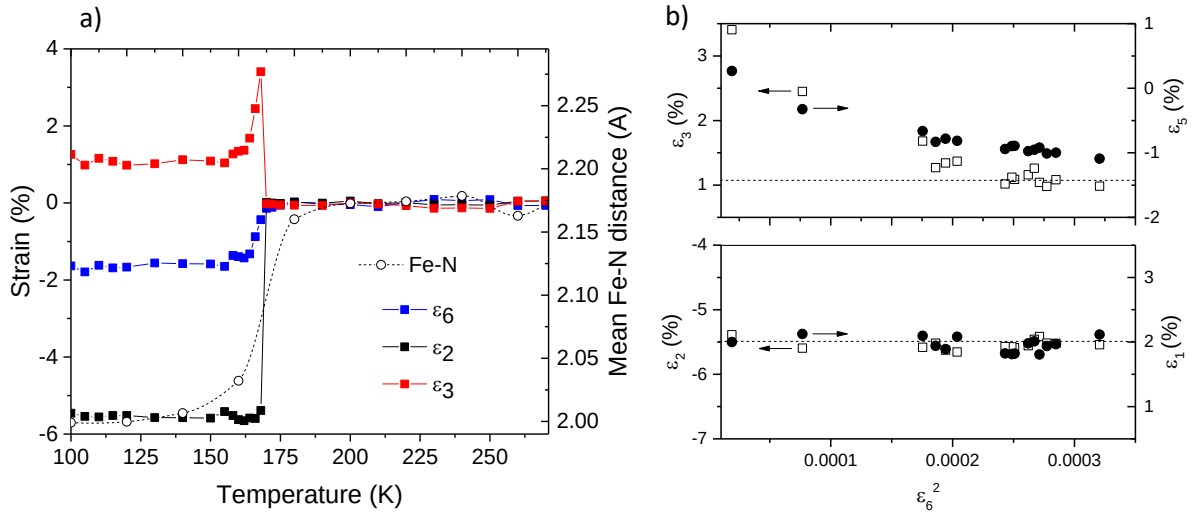

Figure 7. (a) Selected components of the spontaneous strain tensor (ε_i) and mean Fe-N distance as a function of the temperature in the heating mode in a crystal of **(2)**. (b) Non-symmetry-breaking strains (ε_1, ε_2, ε_3 and ε_5) plotted as a function of the square of a symmetry breaking strain ε_6 in **(2)**. (Lines are guides to the eye.)

First, one can note that the overall volume change (2.5 %) is similar to the bipy-derivative (3 %) and the dilation here is also strongly anisotropic. The three shear strains display similar values between 1 - 2 %. Again, we find a good agreement between the values of $V_s(T)$ obtained directly from the unit cell volume and calculated as $Vs = \varepsilon_1 + \varepsilon_2 + \varepsilon_3$. Contrary to the case of the bipy-derivative, however, the normalized non-symmetry-breaking strain curves, $\varepsilon_{nsb}(T)$, do not superpose to each other, neither to the $\bar{d}_{FeN}(T)$ curve. This is obvious for the case of

ε_3(T), which displays a pronounced peak near the phase transition, but the other $\varepsilon_{nsb}(T)$ components deviate also from proportionality (see Figure 7a and Figure S8). We can understand this finding on the basis of Equation 5a, which denotes an extra contribution of the symmetry-breaking order parameter q_{ferro} to the non-symmetry-breaking strains. The presence of this peak in the $\varepsilon_3(T)$ curve implies also that the SCO and the symmetry-breaking transitions are NOT fully synchronized, despite they occur conjointly. The most likely scenario is that the SCO starts gradually at lower temperatures, seen through the increase of ε_3 above ca. 155 K, followed by an abrupt decrease near 169 K due to the structural transition. This reasoning is further supported by the fact that a sizeable increase of the Fe-N distances occurs between 140 and 160 K, in which range the crystal is still triclinic (Figure S10). It is worth to note also that similar situations have been already encountered in other SCO compounds displaying symmetry breakings.[19]

The analysis of the relationship(s) between the symmetry-breaking strain and the order parameters is less straightforward because, contrary to the SCO, we do not have an independent measure of the ferroelastic order parameter. Nevertheless, by comparing equations 5a and 5b, the expectation would be an affine relationship between ε_{nsb} and ${\varepsilon_{sb}}^2$. As shown in Figure 7b, this expectation is indeed nicely met between ε_1 (or ε_2) and ${\varepsilon_6}^2$. However, Figure 7b reveals also that the expected affine relationships between ε_3 (or ε_5) and ${\varepsilon_6}^2$ are not obeyed near the phase transition temperature. (*N.B.* The same tendencies are observed between ε_{nsb} and ${\varepsilon_4}^2$, which is not shown here). This deviation from the expected strain behavior indicates that the contributions from higher order strain – order parameter coupling terms might be significant.

As discussed above, the most remarkable finding of this study is the observation of the monoclinic LS form in **(2)** under an applied pressure of 0.73 GPa, denoting a sequence of spin-state and structural transitions. This result is clearly shown in Figure 8a displaying the variation of Fe-N average distance together with the reduced-cell lattice parameters *b* and *c* as a function

of pressure. There is a clear evidence for lattice distortion from monoclinic to triclinic only from 0.88 GPa, whereas the variation of Fe-N distances provides an obvious proof for a nearly complete SCO (ca. 75 %) already at 0.73 GPa (highlighted in grey).

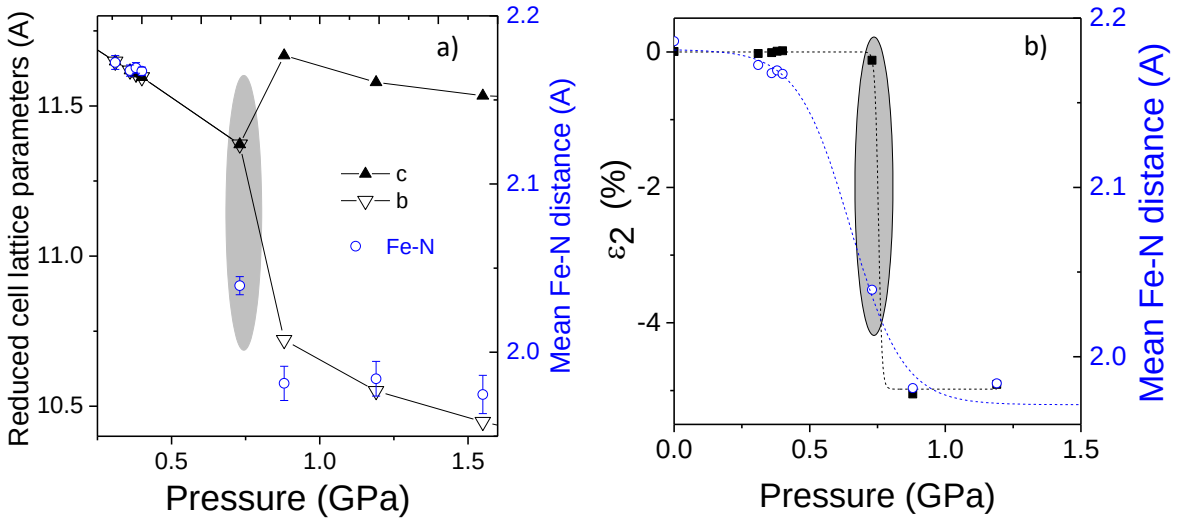

Figure 8. (a) Lattice parameters *b* and *c* of the reduced cell and (b) the spontaneous strain component ε_2 as a function of pressure in **(2)**. The mean Fe-N distance is also shown. (Lines are guides to the eye.) The data highlighted in grey indicate the occurrence of the intermediate, monoclinic LS phase.

Extrapolation of lattice parameters beyond the transition pressure is difficult due to the reduced pressure range and the small amount of data points. For this reason, only the pressure dependence of the ε_2 component of spontaneous strain tensor could be quantified with confidence (Figure 8b). In fact, the coordinate system is chosen such a way that ε_2 is uniquely determined by the modification of the *b* lattice parameter of the reduced cell. As a lucky circumstance, the contraction of *b* at the transition is outstanding, allowing its clear separation from the ordinary response of the crystal to applied pressure. The result is shown in Figure 8b revealing ca. 5.0 % variation of ε_2, which is in fair agreement with the thermally induced value of ca. 5.6 % (Figure 7a), providing thus confidence for our analysis. Strikingly, the value of ε_2

remains zero up to 0.73 GPa and it changes brusquely at the monoclinic (LS) - triclinic (LS) transition at 0.88 GPa (Figure 8b) – although such strain is not predicted from symmetry considerations. We can thus conclude that despite its nearly complete separation from the SCO under pressure, the ferroelastic transition actually remains strongly coupled to it.

At this point, an interesting question emerges concerning the reverse transition upon lowering the pressure. Indeed, the coupling term vanishes if q_{ferro} and/or q_{spin} become zero. This means one should expect rather different SCO behaviors upon compression of the paraelastic phase ($q_{ferro} = 0$) and decompression of the ferroelastic form ($q_{ferro} \neq 0$). As discussed by Collet et al.[19], such asymmetry is a characteristic feature of coupled spin transitions upon heating and cooling. Unfortunately, using our screw-driven DAC, controlled decompression is not straightforward, but such experiments might be possible using double-membrane DACs.

We can rationalize the pressure-induced separation of the two transitions by introducing the work term into Eq. 4,[93] which leads then to (see the SI for more details):

$$\Delta G = \frac{1}{2}a_1\left(T - (T'_{ferro} + \frac{\lambda_{nsb2}P}{Ka_1})\right)q^2{}_{ferro} + \frac{1}{4}b'q^4{}_{ferro} + \frac{1}{4}cq^6{}_{ferro} + A_1[T - (T'_{SCO} - \frac{\lambda_{nsb2}P}{2A_1K})]q_{spin} + \frac{1}{2}B'q^2{}_{spin} + \frac{1}{4}Cq^4{}_{spin} + Dq^2{}_{ferro}q_{spin} \quad (7)$$

First, we note that the coupling of the ferroelastic transition to the non-symmetry-breaking strains of the SCO leads to a strong pressure dependence of the former. The different slopes of the phase transition boundaries are given for the SCO and the ferroelectric transitions, respectively, by:

$$\frac{\partial T_{ferro}}{\partial P} = \frac{\lambda_{nsb2}}{Ka_1} \quad (8a)$$

$$\frac{\partial T_{SCO}}{\partial P} = -\frac{\lambda_{nsb2}}{KA_1} \quad (8b)$$

The experimentally observed Clapeyron slopes (Figure 9) are indeed different for the two transitions. We note also the good agreement with the previously published high-pressure

magnetic measurement data[80] (blue stars in Figure 9). In the high-pressure magnetic data, the hysteresis associated with the SCO disappears between 0.33 and 0.55 GPa, suggesting that the triple point should be near 250 K - 0.4 GPa (shown tentatively by the red circle in Figure 9).[80] On the other hand, the magnetic data revealed also an anomalously large hysteresis near 0.2 GPa and 180 K. The authors suggested this behavior might be linked to the structural transition. Based on our results, we cannot verify this hypothesis. In our opinion, it is more likely that the hysteresis was caused by the solidification of the pressure-transmitting medium (silicon oil) at low temperatures.[60]

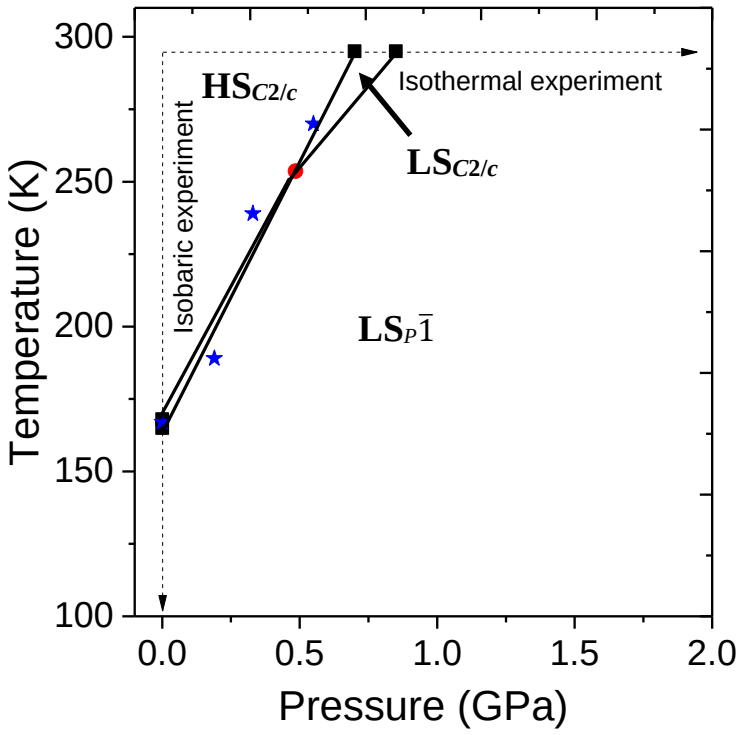

Figure 9. Experimental *P*,*T*-phase diagram showing the stability regions of the different polymorphs of compound **(2)**. Previously published high pressure magnetic data[80] are shown by blue stars. The triple point is shown tentatively by the red circle.

Finally, it is interesting to remark that the HS$_P\bar{1}$ phase does not appear in the *P*,*T*-phase diagram. Indeed, it can be obtained only as a metastable phase following photoexcitation of the LS$_P\bar{1}$

phase at liquid helium temperature where the crystal structure is 'frozen'.[81] As discussed in detail in refs. 19, 32 and 33, the relative stability of the four possible phases depends on the coupling strength *D* and on the difference of the (uncoupled) symmetry-breaking and spin transition temperatures (T_{ferro}-T_{SCO}). Then, the various p,T-phase diagrams can be mapped by assuming a linear dependence of the Landau coefficients *a* and *A* on both *T* and *P*. In general, *D* is assumed to be positive for stabilizing the low-symmetry LS phase. In the case of compound **2**, the intermediate phase is the high-symmetry LS one, which is expected only for coupled transitions and is compatible with T_{ferro}-T_{SCO} < 0. On the other way around, theory shows that T_{ferro}-T_{SCO} > 0 should give rise to an intermediate low-symmetry HS phase.[19] As mentioned before, the latter is indeed the case of compounds $[Fe(ptz)_6](BF)_4$ and $[Co(dpzca)_2]$.[69,73]

CONCLUSIONS

Using high-pressure single crystal x-ray diffraction, we have investigated the elastic coupling mechanism between spin-state and symmetry-breaking structural transitions in the prototype SCO compound $[Fe(H_2B(pz)_2)_2(phen)]$. By the simultaneous assessment of Fe-N distances, i.e. the order parameter (high spin fraction) of the spin transition, and the spontaneous strain components as a function of temperature and pressure, we could gain unprecedented insights into the nature of the coupled phase transition phenomena. Notably, we could unambiguously confirm the theoretically predicted sequence of spin-state and structural transitions at high pressures. In addition, from the analysis of strain behaviors we demonstrated that the 'separated' transitions (at high pressures) remain strongly connected via strain coupling, whereas the 'simultaneous' transitions (at low temperature) remain partially split up. As such, it is preferable to use the term "pressure tuning" instead of "decoupling" of the transitions. A comparison with the related compound $[Fe(H_2B(pz)_2)_2(bipy)]$, showing SCO without symmetry breaking, allowed to clearly highlight the main manifestations of this strain coupling

mechanism. Such HP-SC-XRD observations represent a vital tool for the investigation of coupled phase transitions with relevance to a variety of multifunctional/multiferroic materials – far beyond the scope of SCO phenomenon. The strain-coupling analysis discussed in this paper can be also extended for the analysis of chemical pressure effects[23] as well as substrate effects[94] on SCO films, which is of outmost importance for future applications of SCO materials. Finally, this study serves also to highlight the tremendous progress of high pressure laboratory X-ray diffraction techniques combining large-opening angle DACs with high-flux microfocus sources, low-noise X-ray detectors and highly optimized instrument control software, allowing atomic position resolution of low symmetry triclinic structures under pressure in a reasonable data acquisition time frame (~hours).

ASSOCIATED CONTENT

Supporting Information

The following are available online at ACS Publications website: Supplementary figures and tables (PDF) and movies (AVI).

Accession Codes

Deposition numbers: 2178316-2178353 contain the supplementary crystallographic data for 38 crystal structures at different temperatures and pressures. These data can be obtained free of charge from the CCDC via www.ccdc.cam.ac.uk/data_request/cif.

AUTHOR INFORMATION

Corresponding Author

*e-mail: azzedine.bousseksou@lcc-toulouse.fr & gabor.molnar@lcc-toulouse.fr

Author contributions

The manuscript was written through contributions of all authors.

Notes

The authors declare no competing financial interests.

ACKNOWLEDGMENTS

This work has received funding from the European Research Council (ERC) under the European Union's Horizon 2020 research and innovation programme (grant agreement N° 101019522) as well as from the European Regional Development Fund (ERDF), the Region Occitanie and the company Rigaku Corporation (PRRI project NANOMAT).

REFERENCES

1. Salje, E. (1985). Thermodynamics of sodium feldspar I: order parameter treatment and strain induced coupling effects. Physics and Chemistry of Minerals, 12(2), 93-98.

2. Salje, E., & Devarajan, V. (1986). Phase transitions in systems with strain-induced coupling between two order parameters. Phase Transitions: A multinational Journal, 6(3), 235-247.

3. Carpenter, M. A., Howard, C. J., Kennedy, B. J., & Knight, K. S. (2005). Strain mechanism for order-parameter coupling through successive phase transitions in $PrAlO_3$. Physical Review B, 72(2), 024118.

4. Eerenstein, W., Mathur, N. D., & Scott, J. F. (2006). Multiferroic and magnetoelectric materials. Nature, 442(7104), 759-765.

5. Piekarz, P., Parlinski, K., & Oleś, A. M. (2007). Origin of the Verwey transition in magnetite: Group theory, electronic structure, and lattice dynamics study. Physical Review B, 76(16), 165124.

6. Wang, K. F., Liu, J. M., & Ren, Z. F. (2009). Multiferroicity: the coupling between magnetic and polarization orders. Advances in Physics, 58(4), 321-448.

7. Shatruk, M., Phan, H., Chrisostomo, B. A., & Sulaimenova, A. (2015). Symmetry-breaking structural phase transitions in spin crossover complexes. Coordination Chemistry Reviews, 289-290, 62-73.

8. Salje, E. K. H., & Carpenter, M. A. (2011). Linear–quadratic order parameter coupling and multiferroic phase transitions. Journal of Physics: Condensed Matter, 23(46), 462202.

9. Cointe, M. B. L., Collet, E., Toudic, B., Czarnecki, P., & Cailleau, H. (2017). Back to the structural and dynamical properties of neutral-ionic phase transitions. Crystals, 7(10), 285.

10. Kalcheim, Y., Butakov, N., Vargas, N. M., Lee, M. H., Del Valle, J., Trastoy, J., ... & Schuller, I. K. (2019). Robust coupling between structural and electronic transitions in a mott material. Physical Review Letters, 122(5), 057601.

11. Azzolina, G., Bertoni, R., Ecolivet, C., Tokoro, H., Ohkoshi, S. I., & Collet, E. (2020). Landau theory for non-symmetry-breaking electronic instability coupled to symmetry-breaking order parameter applied to Prussian blue analog. Physical Review B, 102(13), 134104.

12. Carpenter, M. A., Salje, E. K., & Graeme-Barber, A. (1998). Spontaneous strain as a determinant of thermodynamic properties for phase transitions in minerals. European Journal of Mineralogy, 621-691.

13. Gütlich, P., Hauser, A., & Spiering, H. (1994). Thermal and optical switching of iron (II) complexes. Angewandte Chemie International Edition in English, 33(20), 2024-2054.

14. Spiering, H., Boukheddaden, K., Linares, J., & Varret, F. (2004). Total free energy of a spin-crossover molecular system. Physical Review B, 70(18), 184106.

15. Halcrow, M. A. (2011). Structure: function relationships in molecular spin-crossover complexes. Chemical Society Reviews, 40(7), 4119-4142.

16. Guionneau, P. (2014). Crystallography and spin-crossover. A view of breathing materials. Dalton Transactions, 43(2), 382-393.

17. Collet, E., & Guionneau, P. (2018). Structural analysis of spin-crossover materials: From molecules to materials. Comptes Rendus Chimie, 21(12), 1133-1151.

18. Pillet, S. (2021). Spin-crossover materials: Getting the most from x-ray crystallography. Journal of Applied Physics, 129(18), 181101.

19. Collet, E., & Azzolina, G. (2021). Coupling and decoupling of spin crossover and ferroelastic distortion: Unsymmetric hysteresis loop, phase diagram, and sequence of phases. Physical Review Materials, 5(4), 044401.

20. Wiehl, L (1993). Structures of hexakis(1-propyltetrazole)iron(II)bis(tetrafluoroborate), $[Fe(CHN_4C_3H_7)_6](BF_4)_2$, hexakis(1-methyltetrazole)iron(II)bis(tetrafluoroborate), $[Fe(CHN_4CH_3)_6](BF_4)_2$, and the analogous perchlorates. Their relation to spin crossover behaviour and comparison of Debye–Waller factors from structure determination and Mössbauer spectroscopy. Acta Crystallographica Section B: Structural Science, 49(2), 289-303.

21. Kusz, J., Zubko, M., Neder, R. B., & Gütlich, P. (2012). Structural phase transition to disorder low-temperature phase in $[Fe(ptz)_6](BF_4)_2$ spin-crossover compounds. Acta Crystallographica Section B: Structural Science, 68(1), 40-56.

22. Chernyshov, D., Hostettler, M., Törnroos, K. W., & Bürgi, H. B. (2003). Ordering Phenomena and Phase Transitions in a Spin-Crossover Compound—Uncovering the Nature of the Intermediate Phase of $[Fe\ (2\text{-}pic)_3]Cl_2 \cdot EtOH$. Angewandte Chemie International Edition, 42(32), 3825-3830.

23. Jeftić, J., Romstedt, H., & Hauser, A. (1996). The interplay between the spin transition and the crystallographic phase transition in the fe (II) spin-crossover system $[Zn_{1-x}Fe_x(ptz)_6](BF_4)_2$ (x = 0.1, 1; ptz = 1-propyltetrazole). Journal of Physics and Chemistry of Solids, 57(11), 1743-1750.

24. Real, J. A., Bolvin, H., Bousseksou, A., Dworkin, A., Kahn, O., Varret, F., & Zarembowitch, J. (1992). Two-step spin crossover in the new dinuclear compound $[Fe(bt)(NCS)_2]_2$.bpym, with bt = 2,2'-bi-2-thiazoline and bpym = 2,2'-bipyrimidine: experimental investigation and theoretical approach. Journal of the American Chemical Society, 114(12), 4650-4658.

25. Törnroos, K. W., Hostettler, M., Chernyshov, D., Vangdal, B., & Bürgi, H. B. (2006). Interplay of spin conversion and structural phase transformations: re-entrant phase transitions in the 2-propanol solvate of tris(2-picolylamine)iron(II)dichloride. Chemistry–A European Journal, 12(24), 6207-6215.

26. Bousseksou, A., Nasser, J., Linares, J., Boukheddaden, K., & Varret, F. (1992). Ising-like model for the two-step spin-crossover. Journal De Physique I, 2(7), 1381-1403.

27. Bousseksou, A., Varret, F., & Nasser, J. (1993). Ising-like model for the two step spin-crossover of binuclear molecules. Journal de Physique I, 3(6), 1463-1473.

28. Chernyshov, D., Klinduhov, N., Törnroos, K. W., Hostettler, M., Vangdal, B., & Bürgi, H. B. (2007). Coupling between spin conversion and solvent disorder in spin crossover solids. Physical Review B, 76(1), 014406.

29. Watanabe, H., Tanaka, K., Bréfuel, N., Cailleau, H., Létard, J. F., Ravy, S., ... & Collet, E. (2016). Ordering phenomena of high-spin/low-spin states in stepwise spin-crossover materials described by the ANNNI model. Physical Review B, 93(1), 014419.

30. Cruddas, J., & Powell, B. J. (2020). Structure–property relationships and the mechanisms of multistep transitions in spin crossover materials and frameworks. Inorganic Chemistry Frontiers, 7(22), 4424-4437.

31. Slimani, A., & Boukheddaden, K. (2021). Microscopic electroelastic modeling of a spin transition with symmetry breaking. Journal of Applied Physics, 129(17), 173901.

32. Chernyshov, D., Bürgi, H. B., Hostettler, M., & Törnroos, K. W. (2004). Landau theory for spin transition and ordering phenomena in Fe(II) compounds. Physical Review B, 70(9), 094116.

33. Azzolina, G., Bertoni, R., & Collet, E. (2021). General Landau theory of non-symmetry-breaking and symmetry-breaking spin transition materials. Journal of Applied Physics, 129(8), 085106.

34. Seredyuk, M., Gaspar, A. B., Ksenofontov, V., Galyametdinov, Y., Kusz, J., & Gütlich, P. (2008). Iron(II) metallomesogens exhibiting coupled spin state and liquid crystal phase transitions near room temperature. Advanced Functional Materials, 18(14), 2089-2101.

35. Akiyoshi, R., Komatsumaru, Y., Donoshita, M., Dekura, S., Yoshida, Y., Kitagawa, H., ... & Hayami, S. (2021). Ferroelectric and Spin Crossover Behavior in a Cobalt(II) Compound Induced by Polar-Ligand-Substituent Motion. Angewandte Chemie, 133(23), 12827-12832.

36. Jakobsen, V. B., Trzop, E., Dobbelaar, E., Gavin, L. C., Chikara, S., Ding, X., ... & Morgan, G. G. (2021). Domain Wall Dynamics in a Ferroelastic Spin Crossover Complex with Giant Magnetoelectric Coupling. J. Am. Chem. Soc. 144, 1, 195–211.

37. Książek, M., Weselski, M., Kaźmierczak, M., Tołoczko, A., Siczek, M., Durlak, P., ... & Bronisz, R. (2020). Spatiotemporal Studies of the One-Dimensional Coordination Polymer $[Fe(ebtz)_2(C_2H_5CN)_2](BF4)_2$: Tug of War between the Nitrile Reorientation Versus Crystal Lattice as a Tool for Tuning the Spin Crossover Properties. Chemistry–A European Journal, 26(63), 14419-14434.

38. Weselski, M., Książek, M., Mess, P., Kusz, J., & Bronisz, R. (2019). “Normal” and “reverse” spin crossover induced by two different structural events in iron(ii) coordination polymer. Chemical Communications, 55(49), 7033-7036.

39. Jakobsen, V. B., Trzop, E., Gavin, L. C., Dobbelaar, E., Chikara, S., Ding, X., ... & Morgan, G. G. (2020). Stress-induced Domain Wall Motion in a Ferroelastic Mn^{3+} Spin Crossover Complex. Angewandte Chemie, 132(32), 13407-13414.

40. Jornet-Mollá, V., Giménez-Saiz, C., Cañadillas-Delgado, L., Yufit, D. S., Howard, J. A., & Romero, F. M. (2021). Interplay between spin crossover and proton migration along short strong hydrogen bonds. Chemical science, 12(3), 1038-1053.

41. Romero-Morcillo, T., Seredyuk, M., Muñoz, M. C., & Real, J. A. (2015). Meltable spin transition molecular materials with tunable Tc and hysteresis loop width. Angewandte Chemie International Edition, 54(49), 14777-14781.

42. Valverde-Muñoz, F. J., Seredyuk, M., Muñoz, M. C., Molnár, G., Bibik, Y. S., & Real, J. A. (2020). Thermochromic meltable materials with reverse spin transition controlled by chemical design. Angewandte Chemie, 132(42), 18791-18797.

43. Akiyoshi, R., Ohtani, R., Lindoy, L. F., & Hayami, S. (2021). Spin crossover phenomena in long chain alkylated complexes. Dalton Transactions, 50(15), 5065-5079.

44. Kühne, I. A., Barker, A., Zhang, F., Stamenov, P., O'Doherty, O., Müller-Bunz, H., ... & Morgan, G. G. (2020). Modulation of Jahn–Teller distortion and electromechanical response in a Mn^{3+} spin crossover complex. Journal of Physics: Condensed Matter, 32(40), 404002.

45. Valverde-Muñoz, F. J., Seredyuk, M., Meneses-Sánchez, M., Muñoz, M. C., Bartual-Murgui, C., & Real, J. A. (2019). Discrimination between two memory channels by molecular alloying in a doubly bistable spin crossover material. Chemical science, 10(13), 3807-3816.

46. Piñeiro-López, L., Valverde-Muñoz, F. J., Trzop, E., Muñoz, M. C., Seredyuk, M., Castells-Gil, J., ... & Real, J. A. (2021). Guest induced reversible on–off switching of elastic frustration in a 3D spin crossover coordination polymer with room temperature hysteretic behaviour. Chemical science, 12(4), 1317-1326.

47. Gütlich, P., Ksenofontov, V., & Gaspar, A. B. (2005). Pressure effect studies on spin crossover systems. Coordination chemistry reviews, 249(17-18), 1811-1829.

48. Gaspar, A. B., Molnár, G., Rotaru, A., & Shepherd, H. J. (2018). Pressure effect investigations on spin-crossover coordination compounds. Comptes Rendus Chimie, 21(12), 1095-1120.

49. Guionneau, P., & Collet, E. (2013). Piezo-and Photo-Crystallography Applied to Spin-Crossover Materials. In 'Spin-Crossover Materials: Properties and Applications' (Ed. M. A. Halcrow), pp 507-526.

50. Granier, T., Gallois, B., Gaultier, J., Real, J. A., & Zarembowitch, J. (1993). High-pressure single-crystal x-ray diffraction study of two spin-crossover iron (II) complexes: $Fe(Phen)_2(NCS)_2$ and $Fe(Btz)_2(NCS)_2$. Inorganic Chemistry, 32(23), 5305-5312.

51. Guionneau, P., Brigouleix, C., Barrans, Y., Goeta, A. E., Létard, J. F., Howard, J. A., ... & Chasseau, D. (2001). High pressure and very low temperature effects on the crystal structures of some iron(II) complexes. Comptes Rendus de l'Académie des Sciences-Series IIC-Chemistry, 4(2), 161-171.

52. Guionneau, P., Le Pévelen, D., Marchivie, M., Pechev, S., Gaultier, J., Barrans, Y., & Chasseau, D. (2004). Laboratory high-pressure single-crystal X-ray diffraction - Recent improvements and examples of studies. Journal of Physics: Condensed Matter, 16(14), S1151.

53. Guionneau, P., Marchivie, M., Garcia, Y., Howard, J. A., & Chasseau, D. (2005). Spin crossover in [Mn^{III}(pyrol)$_3$tren] probed by high-pressure and low-temperature x-ray diffraction. Physical Review B, 72(21), 214408.

54. Papanikolaou, D., Kosaka, W., Margadonna, S., Kagi, H., Ohkoshi, S. I., & Prassides, K. (2007). Piezomagnetic behavior of the spin crossover Prussian blue analogue CsFe[$Cr(CN)_6$]. The Journal of Physical Chemistry C, 111(22), 8086-8091.

55. Shepherd, H. J., Palamarciuc, T., Rosa, P., Guionneau, P., Molnár, G., Létard, J. F., & Bousseksou, A. (2012). Antagonism between extreme negative linear compression and spin crossover in [$Fe(dpp)_2(NCS)_2$]·py. Angewandte Chemie International Edition, 51(16), 3910-3914.

56. Tissot, A., Shepherd, H. J., Toupet, L., Collet, E., Sainton, J., Molnár, G., ... & Boillot, M. L. (2013). Temperature-and Pressure-Induced Switching of the Molecular Spin State of an Orthorhombic Iron(III) Spin-Crossover Salt. European Journal of Inorganic Chemistry, 2013(5-6), 1001-1008.

57. Pinkowicz, D., Rams, M., Mišek, M., Kamenev, K. V., Tomkowiak, H., Katrusiak, A., & Sieklucka, B. (2015). Enforcing multifunctionality: a pressure-induced spin-crossover photomagnet. Journal of the American chemical society, 137(27), 8795-8802.

58. Paradis, N., Le Gac, F., Guionneau, P., Largeteau, A., Yufit, D. S., Rosa, P., ... & Chastanet, G. (2016). Effects of Internal and External Pressure on the [$Fe(PM\text{-}PEA)_2(NCS)_2$] Spin-Crossover Compound (with PM-PEA= N-(2′-pyridylmethylene)-4-(phenylethynyl) aniline). Magnetochemistry, 2(1), 15.

59. Parisiades, P., Payre, C., Gonzales, J. P., Laborier, J. L., Bidet, J. P., Guionneau, P., ... & Lemée-Cailleau, M. H. (2016). Light-irradiation at 700 MPa down to 1.5 K for neutron diffraction. Measurement Science and Technology, 27(4), 047001.

60. Laisney, J., Shepherd, H. J., Rechignat, L., Molnár, G., Rivière, E., & Boillot, M. L. (2018). Pressure-induced switching properties of the iron (iii) spin-transition complex [Fe^{III}(3-OMeSalEen)$_2$]PF_6. Physical Chemistry Chemical Physics, 20(23), 15951-15959.

61. Mikolasek, M., Manrique-Juarez, M. D., Shepherd, H. J., Ridier, K., Rat, S., Shalabaeva, V., ... & Bousseksou, A. (2018). Complete set of elastic moduli of a spin-crossover solid: Spin-state dependence and mechanical actuation. Journal of the American Chemical Society, 140(28), 8970-8979.

62. Vallone, S. P., Tantillo, A. N., Dos Santos, A. M., Molaison, J. J., Kulmaczewski, R., Chapoy, A., ... & Sandeman, K. G. (2019). Giant barocaloric effect at the spin crossover transition of a molecular crystal. Advanced Materials, 31(23), 1807334.

63. Li, R., Levchenko, G., Valverde-Muñoz, F. J., Gaspar, A. B., Ivashko, V. V., Li, Q., ... & Real, J. A. (2021). Pressure Tunable Electronic Bistability in Fe(II) Hofmann-like Two-Dimensional Coordination Polymer [$Fe(Fpz)_2Pt(CN)_4$]: A Comprehensive Experimental and Theoretical Study. Inorganic chemistry, 60(21), 16016-16028.

64. Romanini, M., Wang, Y., Gürpinar, K., Ornelas, G., Lloveras, P., Zhang, Y., ... & Mañosa, L. (2021). Giant and Reversible Barocaloric Effect in Trinuclear Spin-Crossover Complex $Fe_3(bntrz)_6(tcnset)_6$. Advanced Materials, 33(10), 2008076.

65. Seo, J., Braun, J. D., Dev, V. M., & Mason, J. A. (2022). Driving Barocaloric Effects in a Molecular Spin-Crossover Complex at Low Pressures. Journal of the American Chemical Society, 144(14), 6493-6503.

66. Rodríguez-Velamazán, J. A., Canadillas-Delgado, L., Castro, M., McIntyre, G. J., & Real, J. A. (2014). Temperature-and pressure-dependent structural study of $\{Fe(pmd)_2[Ag(CN)_2]_2\}_n$ spin-crossover compound by neutron Laue diffraction. Acta Crystallographica Section B: Structural Science, Crystal Engineering and Materials, 70(3), 436-443.

67. Lemée-Cailleau, M. H., Ecolivet, C., Ouladdiaf, B., Moussa, F., Jeftic, J., & Létard, J. F. (2007). Intermediate ferroelastic phase of the photo-sensible spin-crossover system $[Fe(ptz)_6](BF_4)_2$. Journal of magnetism and magnetic materials, 310(2), 1792-1793.

68. Legrand, V., Le Gac, F., Guionneau, P., & Létard, J. F. (2008). Neutron powder diffraction studies of two spin transition FeII complexes under pressure. Journal of Applied Crystallography, 41(3), 637-640.

69. Lemée-Cailleau, M. H., Ecolivet, C., Ouladdiaf, B., Moussa, F., & Létard, J. F. (2009). Multi-phase spin crossover in $Fe(ptz)_6(BF_4)_2$. Physica B: Condensed Matter, 404(3-4), 379-381.

70. Shepherd, H. J., Bonnet, S., Guionneau, P., Bedoui, S., Garbarino, G., Nicolazzi, W., ... & Molnár, G. (2011). Pressure-induced two-step spin transition with structural symmetry breaking: X-ray diffraction, magnetic, and Raman studies. Physical Review B, 84(14), 144107.

71. Shepherd, H. J., Rosa, P., Vendier, L., Casati, N., Létard, J. F., Bousseksou, A., ... & Molnár, G. (2012). High-pressure spin-crossover in a dinuclear Fe(II) complex. Physical Chemistry Chemical Physics, 14(15), 5265-5271.

72. Legrand, V., Pechev, S., Létard, J. F., & Guionneau, P. (2013). Synergy between polymorphism, pressure, spin-crossover and temperature in $[Fe(PM\text{-}BiA)_2(NCS)_2]$: A neutron powder diffraction investigation. Physical Chemistry Chemical Physics, 15(33), 13872-13880.

73. Miller, R. G., Narayanaswamy, S., Clark, S. M., Dera, P., Jameson, G. B., Tallon, J. L., & Brooker, S. (2015). Pressure induced separation of phase-transition-triggered-abrupt vs. gradual components of spin crossover. Dalton Transactions, 44(48), 20843-20849.

74. Shepherd, H. J., Tonge, G., Hatcher, L. E., Bryant, M. J., Knichal, J. V., Raithby, P. R., ... & Teat, S. J. (2016). A high pressure investigation of the order-disorder phase transition and accompanying spin crossover in $[FeL1_2](ClO_4)_2$ (L1 = 2,6-bis{3-methylpyrazol-1-yl}-pyrazine). Magnetochemistry, 2(1), 9.

75. Weselski, M., Książek, M., Kusz, J., Białońska, A., Paliwoda, D., Hanfland, M., ... & Bronisz, R. (2017). Evidence of Ligand Elasticity Occurring in Temperature-, Light-, and Pressure-Induced Spin Crossover in 1D Coordination Polymers $[Fe(3ditz)_3]X_2$ (X= ClO_4^-, BF_4^-). European Journal of Inorganic Chemistry, 2017(8), 1171-1179.

76. Tailleur, E., Marchivie, M., Itié, J. P., Rosa, P., Daro, N., & Guionneau, P. (2018). Pressure-Induced Spin-Crossover Features at Variable Temperature Revealed by In Situ Synchrotron Powder X-ray Diffraction. Chemistry–A European Journal, 24(54), 14495-14499.

77. Turner, G. F., Campbell, F., Moggach, S. A., Parsons, S., Goeta, A. E., Muñoz, M. C., & Real, J. A. (2020). Single-Crystal X-Ray Diffraction Study of Pressure and Temperature-Induced Spin Trapping in a Bistable Iron(II) Hofmann Framework. Angewandte Chemie International Edition, 59(8), 3106-3111.

78. Real, J. A., Muñoz, M. C., Faus, J., & Solans, X. (1997). Spin crossover in novel Dihydrobis(1-pyrazolyl)borate $[H_2B(pz)_2]$ - containing Iron(II) complexes. Synthesis, X-ray

structure, and magnetic properties of [FeL{$H_2B(pz)_2$}$_2$] (L = 1,10-Phenanthroline and 2, 2'-Bipyridine). Inorganic Chemistry, 36(14), 3008-3013.

79. Moliner, N., Salmon, L., Capes, L., Munoz, M. C., Létard, J. F., Bousseksou, A., ... & Real, J. A. (2002). Thermal and optical switching of molecular spin states in the {[FeL[$H_2B(pz)_2$]$_2$} spin-crossover system (L = bpy, phen). The Journal of Physical Chemistry B, 106(16), 4276-4283.

80. Galet, A., Gaspar, A. B., Agusti, G., Muñoz, M. C., Levchenko, G., & Real, J. A. (2006). Pressure effect investigations on the spin crossover systems {Fe[$H_2B(pz)_2$]$_2$(bipy)} and {Fe[$H_2B(pz)_2$]$_2$(phen)}. Eur. J. Inorg. Chem. 3571-3573.

81. Thompson, A. L., Goeta, A. E., Real, J. A., Galet, A., & Munoz, M. C. (2004). Thermal and light induced polymorphism in iron(II) spin crossover compounds. Chemical communications, (12), 1390-1391.

82. Piermarini, G. J., Block, S., Barnett, J. D., & Forman, R. A. (1975). Calibration of the pressure dependence of the R1 ruby fluorescence line to 195 kbar. Journal of Applied Physics, 46(6), 2774-2780.

83. Tateiwa, N., & Haga, Y. (2009). Evaluations of pressure-transmitting media for cryogenic experiments with diamond anvil cell. Review of Scientific Instruments, 80(12), 123901.

84. CrysAlisPro, Oxford Diffraction Ltd., Version 1.171.33.66.

85. Sheldrick, G. M. (2008). A short history of SHELX. Acta Crystallographica Section A: Foundations of Crystallography, 64(1), 112-122.

86. Salje E K (1993). Phase Transitions in Ferroelastic and Co-elastic Crystals (Cambridge: Cambridge University Press).

87. EOS-FIT 5.2. R. J. Angel, Equations of State, in High-pressure, high-temperature crystal chemistry. Reviews in mineralogy and geochemistry, ed. R. M. Hazen and R. T. Downs, 2001, vol. 41, p. 35.

88. Rat, S., Mikolasek, M., Costá, J. S., Chumakov, A. I., Nicolazzi, W., Molnár, G., ... & Bousseksou, A. (2016). Raman and nuclear inelastic scattering study of the lattice dynamics of the [Fe ($H_2B(pz)_2$)$_2$(phen)] spin crossover complex. Chemical Physics Letters, 653, 131-136.

89. Nye, J. F. (1985). Physical properties of crystals: their representation by tensors and matrices. Oxford University Press.

90. Mason, H. E., Li, W., Carpenter, M. A., Hamilton, M. L., Howard, J. A., & Sparkes, H. A. (2016). Structural and spectroscopic characterisation of the spin crossover in [Fe(abpt)$_2$(NCS)$_2$] polymorph A. New Journal of Chemistry, 40(3), 2466-2478.

91. Toledano, P., & Toledano, J. C. (1987). Landau Theory Of Phase Transitions, The: Application To Structural, Incommensurate, Magnetic And Liquid Crystal Systems (Vol. 3). World Scientific Publishing Company.

92. Camara, F., Carpenter, M. A., Domeneghetti, M. C., & Tazzoli, V. (2003). Coupling between non-convergent ordering and transition temperature in the C2/c↔ P21/c phase transition in pigeonite. American Mineralogist, 88(7), 1115-1128.

93. Angel, R. J. (2000). High-pressure structural phase transitions. Reviews in Mineralogy and Geochemistry, 39(1), 85-104.

94. Pertsev, N. A., Tagantsev, A. K., & Setter, N. (2000). Phase transitions and strain-induced ferroelectricity in $SrTiO_3$ epitaxial thin films. Physical Review B 61(2), R825-R829.

For Table of Contents Only

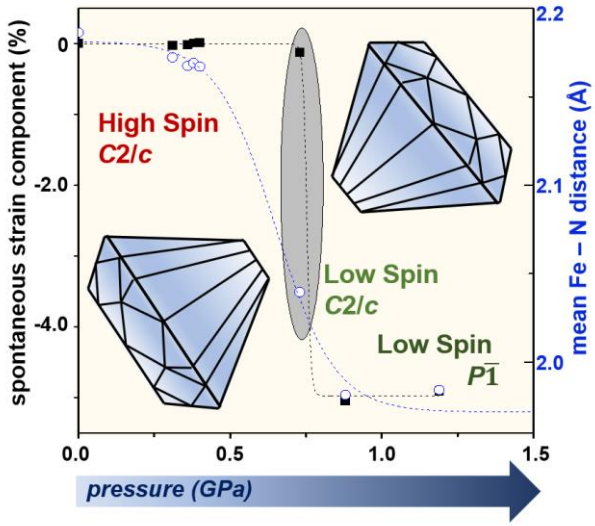

Using low-temperature and high-pressure single crystal x-ray diffraction, we have investigated the strain coupling mechanism between the spin-state and symmetry-breaking structural transitions in the compound $[Fe(H_2B(pz)_2)_2(phen)]$. By the simultaneous assessment of Fe-N distances and the spontaneous strain components, we could gain unprecedented insights into the coupling of the order parameters. Notably, we could unambiguously confirm the theoretically predicted sequence of spin-state and structural transitions at high pressures.